Available online at www.sciencedirect.com

SciVerse ScienceDirect

Ceramics International 38 (2012) 4345–4352

CERAMICS INTERNATIONAL

www.elsevier.com/locate/ceramint

Ruddlesden–Popper structured $BaLa_2Ti_3O_{10}$, a highly anisotropic material for thermal barrier coatings

Lei Guo [a], Hongbo Guo [a,b,*], Guohui Ma [a], Musharaf Abbas [a], Shengkai Gong [a,b]

[a] School of Materials Science and Engineering, Beihang University, No. 37 Xueyuan Road, Beijing 100191, China
[b] Key Laboratory of Aerospace Materials and Performance (Ministry of Education), China

Received 3 December 2011; received in revised form 7 February 2012; accepted 7 February 2012
Available online 14 February 2012

Abstract

$BaLa_2Ti_3O_{10}$ (BLT) with Ruddlesden–Popper structure is investigated as a material for thermal barrier coatings (TBCs). BLT shows excellent sintering resistance and remains phase stability at 1500 °C for 110 h. After annealing at 1500 °C for 1 h, BLT bulk material exhibits *c*-axis textured structure with *c*-axis parallel to the hot pressing direction. Thermal expansion coefficients of BLT in *a–b* plane are in the range of 9.5×10^{-6}–11.3×10^{-6} K^{-1}, whereas those along *c*-axis range from 10.4×10^{-6} to 12.1×10^{-6} K^{-1}, which are comparable to those of 8YSZ. The thermal conductivities of BLT in *a–b* plane and along *c*-axis are 1.41–1.71 and 1.31–1.60 W/mK, respectively, nearly 20% lower than those of 8YSZ. The anisotropy in thermo-physical properties is attributed to the insertion of weakly bonded Ba–O layer in the BLT crystal.

Keywords: C. Thermal properties; E. Thermal applications; $BaLa_2Ti_3O_{10}$ (BLT); Anisotropy

1. Introduction

In order to increase the gas turbine inlet temperatures and protect the hot components of gas turbines against high temperature oxidation and hot corrosion, thermal barrier coatings (TBCs) have been investigated and developed since their first application in the early 1960s [1,2]. Commonly, electron-beam physical vapor deposition (EB-PVD) and plasma spraying (PS) techniques are used to produce TBCs. Because of high thermal expansion coefficient and low thermal conductivity, 7–8 wt% Y_2O_3 stabilized ZrO_2 (YSZ) has been universally used as ceramic TBCs material. However, two flaws has been reported when YSZ are exposed to high temperature (above 1200 °C) for long time, i.e., phase transformation and sintering. Metastable tetragonal phase decomposes into tetragonal and cubic phase above 1200 °C. Upon cooling, tetragonal phase transforms to monoclinic phase, causing about 3.5% volume change and resulting in crack formation in the TBCs [3–5]. In addition, volume fraction of pores decreases due to the significant sintering of YSZ at high temperature, which leads to an increase in the thermal conductivity as well as the in-plane stiffness and thus decreases the strain compliance of TBCs [6,7].

Due to the described shortcomings of YSZ, considerable efforts have been made to seek alternatives to further increase the gas turbine inlet temperature. Previous investigations were mainly focused on fluorite-structured materials due to similar structure with zirconia [8–11], and then attentions were turned to pyrochlore-structured materials because of the close relationship with fluorite-structured materials [12]. Perovskites are another attractive materials class for TBCs application due to their low thermal conductivities [13], good corrosion resistance and low cost [14]. Yamanaka empirically confirmed that $SrHfO_3$ has high melting temperature (2950 °C) and high thermal expansion (11.3×10^{-6} K^{-1}), but the thermal conductivity is somewhat high [15]. Ma et al. reported that dense $SrZrO_3$ has excellent mechanical properties (Young's modulus, hardness, fracture toughness) and the sintering rate of $SrZrO_3$ coating at 1200 °C is less than half that of 8YSZ coating [16].

The ideal perovskite ($A^{2+}B^{4+}O_3$) is in space group *Pm*3*m*, which is commonly visualized as a three-dimensional chain of BX_6 octahedra. The properties of perovskite-structured materials can be selectively influenced by substituting ions

* Corresponding author at: School of Materials Science and Engineering, Beihang University, No. 37 Xueyuan Road, Beijing 100191, China.
Tel.: +86 10 8231 7117; fax: +86 10 8233 8200.
E-mail address: guo.hongbo@buaa.edu.cn (H. Guo).

0272-8842/$36.00
doi:10.1016/j.ceramint.2012.02.017

at A or/and B sites [17]. The most common distortion in perovskites is BX_6 octahedra titling, which allows intermixing of different ions on the same crystallographic sites. However, since the perovskite structure is more rigid than the pyrochlore structure, the thermal conductivities of perovskite-structured materials are not sufficiently low [12]. It is reported that materials with large, complex unit cells should exhibit low thermal conductivity and high thermal expansion coefficient [18]. Therefore, attentions were turned to materials with complex crystal structure [19–21]. In addition, there are growing interests in compounds with superlattice or anisotropic crystal structure. W/Al_2O_3 nanocomposites [22], WSe_2 disordered films [23] and layered perovskites with superlattice structure have been reported to reveal low thermal conductivity. While the perovskite prototype structure is cubic, perovskite-based structures exhibit anisotropies of varying symmetries and degrees. These materials include $Bi_4Ti_3O_{12}$ with the Aurivillis structure [24,25] and $A_{n+1}B_nO_{3n+1}$ (A: RE, Sr; B: Ti, Al) with the Ruddlesden–Popper structure [26,27].

$BaLn_2Ti_3O_{10}$ (Ln: Sm, Nd, Pr, La) crystallizes in the $n = 3$ member of Ruddlesden–Popper structure, which is a perovskite derivative. The structure can be envisioned as a tri-perovskite layer separated by a weakly bonded Ba–O layer along *c*-axis, $BaLn_2Ti_3O_{10}$ therefore show a high degree of crystalline anisotropy, which is one of the most attractive features for $BaLn_2Ti_3O_{10}$ ceramics as TBCs materials. The insertion of weakly bonded Ba–O layer could work as barrier to phonon conduction, thus reducing thermal diffusivity. $BaLn_2Ti_3O_{10}$ exhibits monoclinic and orthorhombic crystal structures, which can be synthesized by high-temperature solid reaction and sol–gel method [28,29]. $BaNd_2Ti_3O_{10}$ was found to exhibit stability and low thermal conductivity over a wide range of temperatures [30]. In our previous work, $BaLa_2Ti_3O_{10}$ (BLT) coatings with nearly stoichiomertric composition has been successfully produced by plasma spray, as seen in Ref. [31], and the thermo-physical and thermal cycling properties of the coatings were investigated. It was found that BLT coating exhibit lower thermal conductivity and better thermal cycling performance compared to the used 8YSZ. It is inspiring that no preferential volatilization of components was found during BLT spraying. In the previous research, low thermal conductivity of BLT was attributed to its weakly bonded planes that exist between planes containing rigid polyhedra in layered oxides [31]. However, the structural characterizations of BLT were not carried out, and the effects of weakly bonded planes on the BLT performance were not identified in detail.

In our previous study, BLT was found to be a promising thermal barrier coatings material, however further investigation were required to exploit its potential for thermal barrier coatings application in a more elaborated form. BLT is an anisotropic material, however, the structural characterization and the relationship between structure and property of BLT have not been reported yet. In the present paper, the crystalline anisotropy of BLT is identified, and *c*-axis textured BLT samples are produced. Simultaneously, the thermo-physical properties of BLT bulk material along *c*-axis and in *a*–*b* plane are compared.

2. Experimental procedures

$BaLa_2Ti_3O_{10}$ (BLT) powders were synthesized through a solid state reaction method. Powders of $BaCO_3$, TiO_2 and La_2O_3 (purity higher than 99.99%) used as raw materials were mechanically mixed in ionized water for 1 h, followed by drying at 160 °C. Subsequently, the mixed powders were calcined at 1500 °C for 48 h. The process was repeated until the pure BLT powders were obtained. BLT bulk materials were produced by hot pressing at 1200 °C with a pressure of 20 MPa for 2 h, and then the bulk materials were annealed at 1500 °C for 1 h to obtain *c*-axis textured structure.

The crystal structure was characterized by X-ray diffraction (XRD, Rigaku Diffractometer, CuKa radiation), and pole figure analysis was carried out to identify the texture of BLT. Cross-section of BLT after annealing was cut normal to hot pressing direction and pole figure measurement was collected for (0 0 3) Bragg peak. The tilt angle was varied from 20° to 90° and a maximum rotation angle was up to 90°. Both tilt angle and the rotation angle were increased in 5° steps. The long periodic modulated structure of BLT was determined by transmission electron microscopy (TEM, JEM-2010). Sample used for the TEM analysis was prepared by first grinding the BLT powders to nanoscale level, and then it was dispersed into ethanol ultrasonically. The grain appearance of BLT was characterized using scanning electron microscope (SEM). BLT samples were cut along hot pressing direction and perpendicular to hot pressing direction. These two cross sections were polished by routine metallographic techniques and then thermally etched (at 1500 °C for 30 min) in order to delineate grain boundaries. These samples were observed in a QUANTA 600 SEM (FEI, Holland) equipped with energy dispersive spectroscopy (EDS, IE 350).

Thermal expansion coefficients (TECs) of BLT were determined using a high-temperature dilatometer (Netzsch DIL 402E, Germany). Due to texture, the TECs of samples in longitudinal direction normal to hot pressing direction (BLT1) and parallel to hot pressing direction (BLT2) were both measured. The samples were machined to 25 mm × 4 mm × 4 mm for measurement.

Thermal conductivities, λ, were evaluated using the equation

$$\lambda = \alpha^{\bullet} C_P^{\bullet} \rho \quad (1)$$

where ρ is the density (kg/m^3), C_p is the specific heat capacity (J/kg K), and α denotes the thermal diffusivity (m^2/s).

Thermal diffusivities were investigated by laser flash diffusivity technique. The thermal diffusivity measurements were carried out on disk-shaped specimens with a diameter 12.7 mm and height 1 mm, using a laser flash device (NetzschLFA427, Germany). Specimen with testing direction parallel to hot pressing direction (BLT3) and normal to hot pressing direction (BLT4) was both machined. Prior to thermal diffusivity measurement, the specimen surfaces were coated with a thin layer of carbon for thermal absorption of laser pulses.

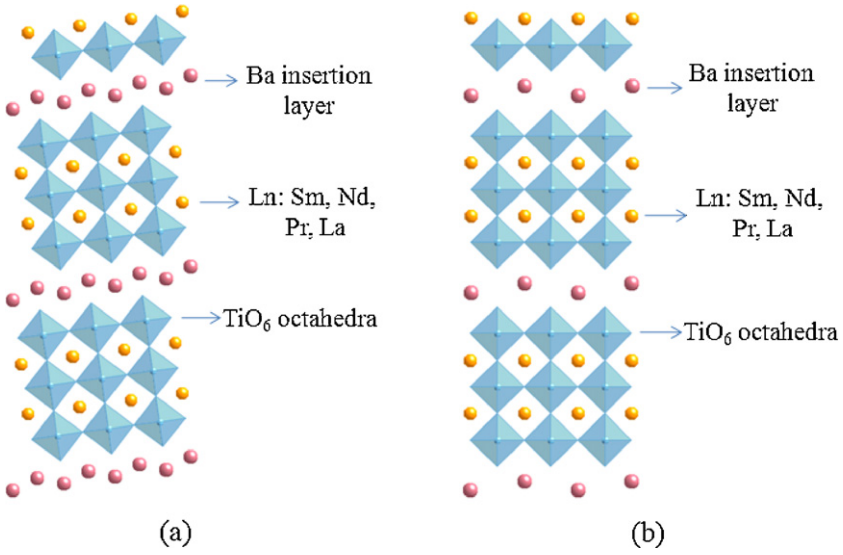

Fig. 1. $BaLn_2Ti_3O_{10}$ (Ln: Sm, Nd, Pr, La) crystal structure model showing a tri-perovskite layer separated by a BaO layer along *c*-axis. (a) (1 0 0) plane, (b) (0 1 0) plane.

Specific heat of the BLT specimen was measured by differential scanning calorimeter (DSC, Netzsch STA 449C, Germany) in argon atmosphere with a heating rate of 20 °C min^{-1}. In addition, specific heat can be calculated based on Neumann–Kopp law [32]:

$$C_{p(\mathrm{BLT})} = C_{p(\mathrm{BaO})} + C_{p(\mathrm{La_2O_3})} + 3C_{p(\mathrm{TiO_2})} \quad (2)$$

where $C_{p(\mathrm{BLT})}$, $C_{p(\mathrm{BaO})}$, $C_{p(\mathrm{La_2O_3})}$ and $C_{p(\mathrm{TiO_2})}$ denote the specific heats of BLT, BaO, La_2O_3 and TiO_2 respectively.

The density varies with temperature [33]. At temperature *T*, it can be calculated by

$$\rho(T) = \frac{\rho_0}{1 + (\alpha_a + \alpha_b + \alpha_c)\Delta T} \quad (3)$$

where ρ_0 is density at room temperature (T_0), ΔT is temperature difference, $\Delta T = T - T_0$, α_a, α_b and α_c denote TECs of crystal along [1 0 0], [0 1 0] and [0 0 1] orientations respectively.

3. Results and discussion

3.1. Synthesis and structural characterization

The XRD pattern of $BaLa_2Ti_3O_{10}$ (BLT) powders by solid state reaction at 1500 °C for 48 h is shown in Fig. 2. The powders are basically composed of monoclinic BLT phase, and the diffraction peaks of BLT are sharp suggesting good crystallization.

The high resolution image of (1 0 0) plane of BLT is presented in Fig. 3. Long periodic modulated structure resulting from orderly insertion of Ba is observed, which agrees with (1 0 0) plane structure model of $BaLn_2Ti_3O_{10}$ as shown in Fig. 1. Well defined high resolution image of BLT was obtained by anti Fourier transform, as shown in Fig. 3b. Orderly stripes are observed in regions A and B along arrows, suggesting long periodic modulated structure. Moreover, it is found that the modulation directions in regions A and B are perpendicular, which can be attributed to the domain structure of BLT. This long periodic modulated structure greatly influences the crystal growth, sintering and thermo-physical properties of BLT, which is discussed later.

Fig. 4a shows the morphology of BLT powders. The size distribution of BLT powders is uniform, mostly less than 5 μm. The fracture section SEM image of BLT bulk material is compared in Fig. 4b, in which no apparent growth of BLT particles is found during hot pressing at 1200 °C. Generally, large particles grow more easily than small particles due to their lower surface energy when sintering occurs [34]. However, large BLT particles almost keep their former appearance even after hot pressing at 1200 °C. It can be inferred that BLT possesses good sintering resistance.

Fig. 5 show the thermally etched cross-section SEM micrographs of BLT bulk material after annealing at 1500 °C for 1 h. Obvious grain growth is found and all grains are almost in contact with each other, indicating nearly

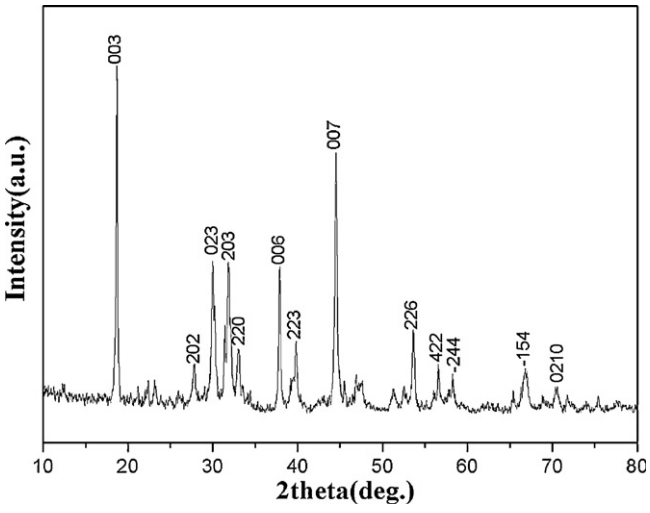

Fig. 2. XRD pattern of BLT powders by solid-state reaction at 1500 °C for 48 h.

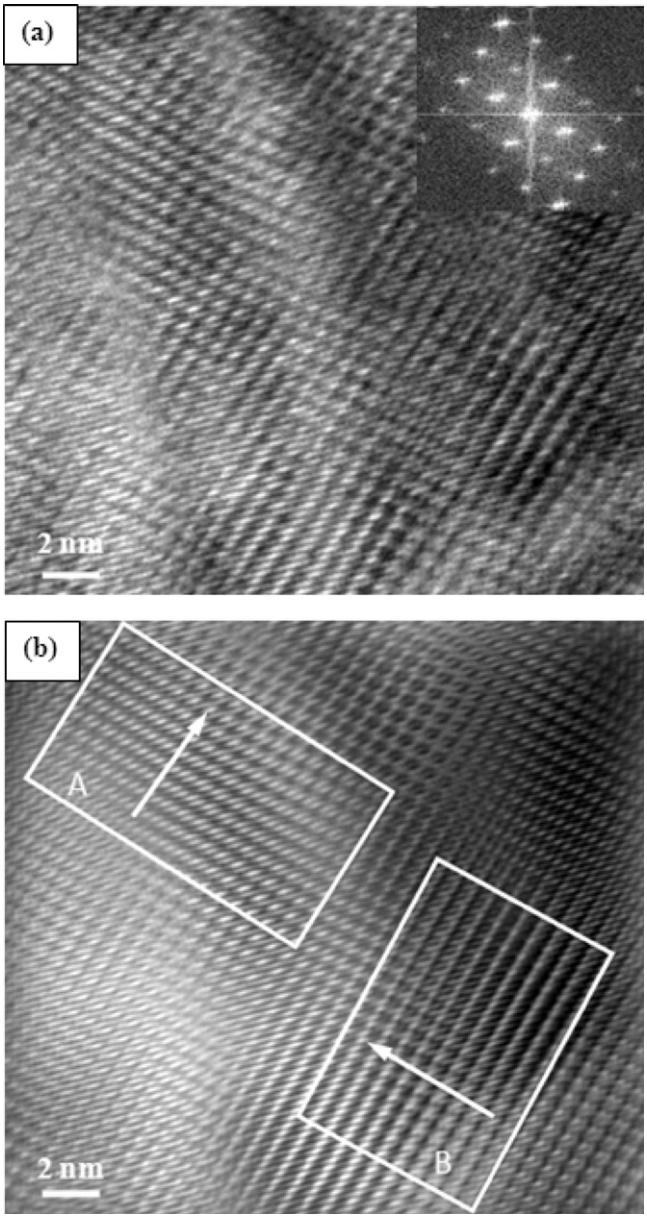

Fig. 3. High resolution image (a) and anti Fourier image of (1 0;0) plane of BLT.

complete sintering. However, the appearance of BLT bulk material in the two mutually perpendicular section planes is greatly different. In the section plane parallel to hot pressing direction as shown in Fig. 5a, the grains exhibit rod-shaped appearance, having high parallelism. While in the section plane normal to the hot pressing direction as shown in Fig. 5b, the grains show irregular shape, and the grain size distribution is heterogeneous, being maximum grain diameter up to 30 μm. According to the SEM micrographs from these two mutually perpendicular section planes, it can be speculated that the grain of BLT exhibits lamellar structure, with thickness direction along hot pressing direction. From the crystal structure model of BLT, orderly Ba insertion layers are found along *c*-axis, the growth rate is therefore lower along *c*-axis than in the *a*–*b* plane, which leads to lamellar structure of BLT grain with thickness direction along *c*-axis after sintering. Therefore, it can be inferred that BLT exhibits *c*-axis textured structure, and the *c*-axis of BLT grain is parallel to hot pressing direction after thermal annealing at 1500 °C for 1 h, which is demonstrated later.

Fig. 6 shows the XRD patterns of BLT bulk material after annealing at 1500 °C for 1 h. In the section plane normal to hot pressing direction, the peak intensities of (0 0 3), (0 0 6) and (0 0 7) are high, while in the section plane parallel to hot pressing direction, (0 2 0), (0 2 3), (2 0 3), (2 2 0), (4 0 1) and (4 2 2) exhibit high peak intensities. This suggests *c*-axis texture of BLT bulk material and indicates that the *c*-axis of BLT bulk material is parallel to the hot pressing direction.

More rigorous description of anisotropy and preferential orientation of BLT was carried out by pole figure analysis. Fig. 7 presents (0 0 3) pole figure and standard pole figure for section plane of BLT bulk material, which is normal to hot pressing direction. It is found that (0 0 3) diffraction peak

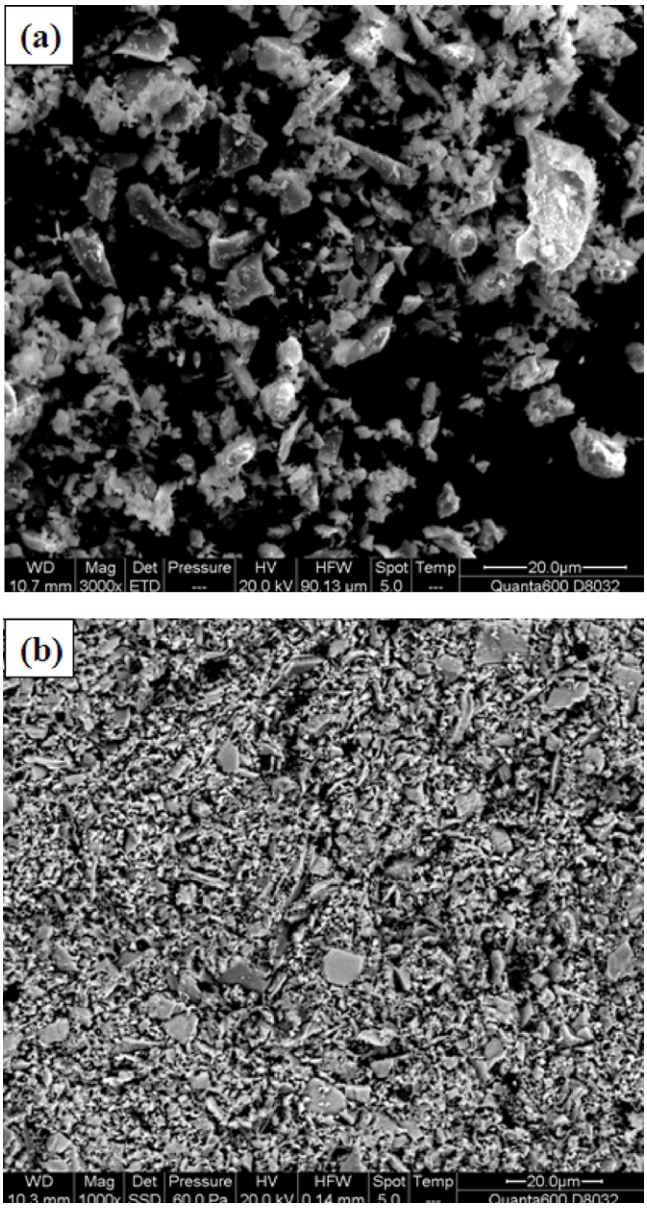

Fig. 4. SEM micrographs of BLT powders (a) and bulk material (b).

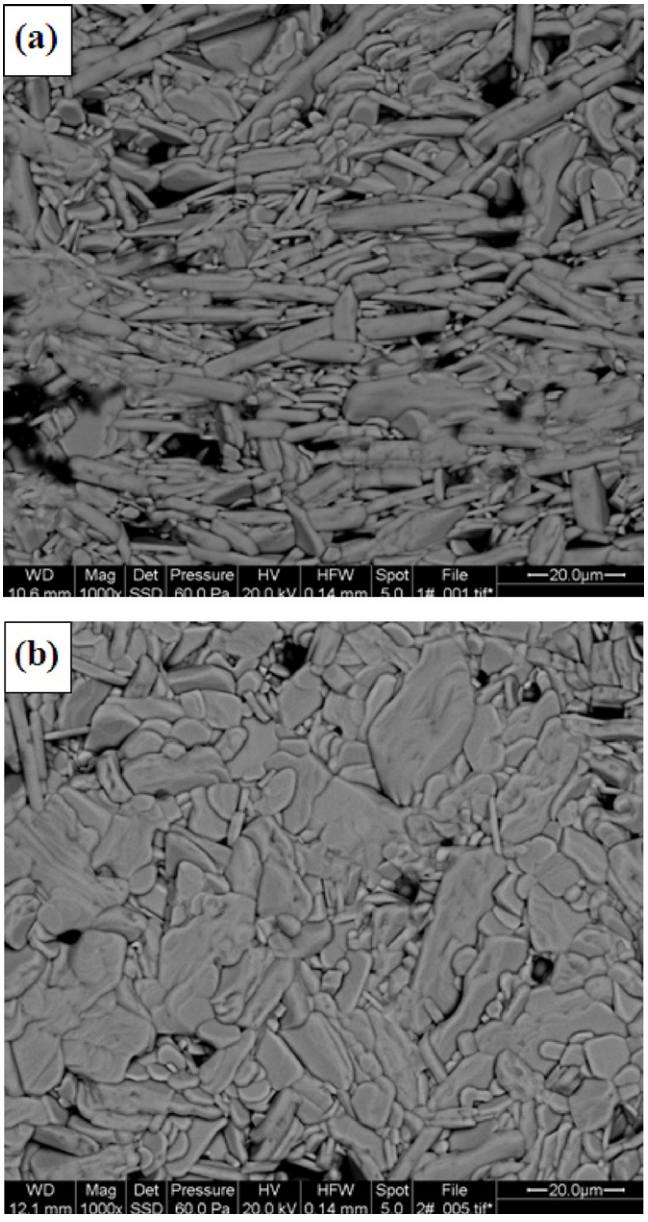

Fig. 5. Thermally etched SEM micrographs of BLT bulk material after annealing at 1500 °C for 1 h. (a) Section plane parallel to hot pressing direction, (b) section plane normal to hot pressing direction.

focuses on the center of projection plane, which agrees well with the standard pole figure, suggesting that (0 0 3) plane is nearly parallel to the section plane and indicating the preferential orientation of (0 0 1). Therefore, it can be inferred that BLT bulk material exhibits *c*-axis textured structure, with *c*-axis parallel to the hot pressing direction, which is consistent with the XRD result.

It can be concluded that the grain of BLT bulk material after thermal annealing exhibits lamellar structure with the thickness direction along *c*-axis, and BLT bulk material shows *c*-axis textured structure with *c*-axis parallel to the hot pressing direction. The effects of crystalline anisotropy on the properties of BLT material are presented in the following part.

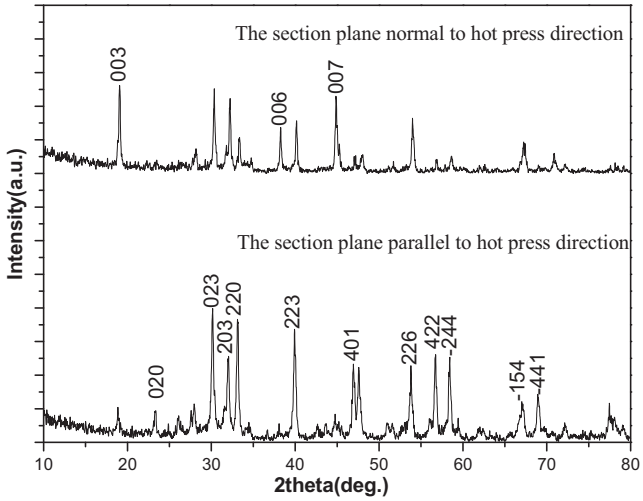

Fig. 6. XRD patterns of BLT bulk material after annealing at 1500 °C for 1 h.

3.2. Thermal stability and thermo-physical properties of BLT

Fig. 8 shows the XRD patterns of BLT recorded at elevated temperatures (25–1100 °C), and XRD pattern of BLT after annealing at 1500 °C for 110 h is also presented. As temperature increases, no diffraction peak splits or disappears, and intensity ratio of BLT peaks almost keeps constant. Due to thermal expansion of crystal lattice, diffraction peaks of BLT move toward low angles with increase in temperature. No obvious change was found in BLT after annealing at 1500 °C for 110 h when compared with as-fabricated BLT. According to the previous structure analysis of BLT, it is presumed that BLT is prone to phase transformation or decomposition due to the insertion of Ba along *c*-axis. However, no phase transformation or decomposition was found during annealing process according to XRD results, implying good thermal stability of BLT. As we know, 8YSZ could not operate over a long time above 1200 °C due to phase transformation, BLT is therefore a better alternative as a material of choice for thermal barrier coating applications due to its better thermal stability.

The thermal expansion coefficients (TECs) of BLT1, BLT2 and 8YSZ are compared in Fig. 9a. It can be seen that the TECs of all the samples increase linearly when heating from room

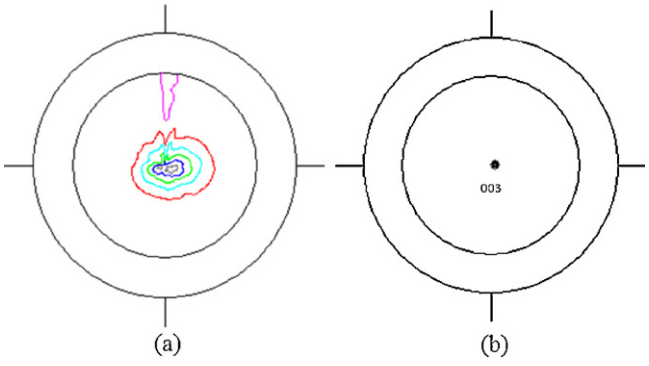

Fig. 7. (0 0 3) pole figure (a) and standard pole (b) of BLT bulk material.

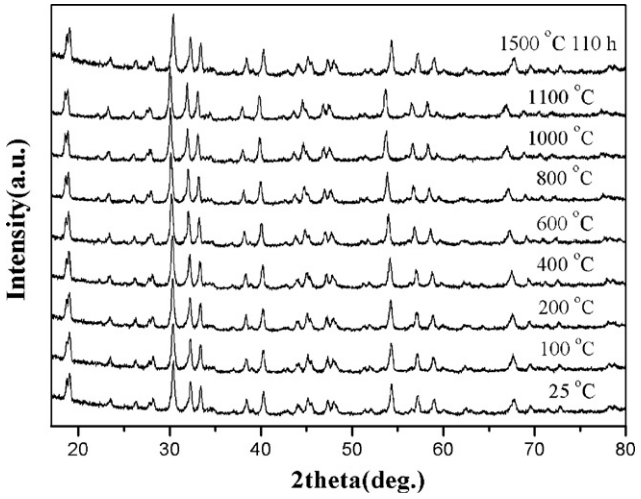

Fig. 8. XRD patterns of BLT at elevated temperatures and after annealing at 1500 °C for 110 h.

temperature to 1200 °C. The values of BLT1 range from 9.5×10^{-6} to 11.3×10^{-6} K^{-1}, whereas those of BLT2 range from 10.4×10^{-6} to 12.1×10^{-6} K^{-1}, which are comparable to those of 8YSZ. The TECs of BLT are larger parallel to hot pressing direction than normal to pressing direction, which is indicative of anisotropy in thermal expansion.

Fig. 9b shows the cell parameters of BLT at various temperatures calculated from XRD patterns in Fig8, and a, b and c represent [1 0 0], [0 1 0] and [0 0 1] orientations respectively. It can be see that cell parameters increase with rising temperature. The slope of cell parameter curve is TEC, so the average TEC of BLT along [0 0 1] is 12.0×10^{-6} K^{-1}, and those along [1 0 0] and [0 1 0] are 9.9×10^{-6} K^{-1} and 9.0×10^{-6} K^{-1} respectively. The calculated average TEC along *c*-axis is larger than those along *a*–*b* plane, suggesting anisotropic thermal expansion of BLT crystal, which is consistent with the measurement results. This anisotropy is attributed to insertion of Ba along *c*-axis. It is known that lattice with weak chemical bond exhibits large thermal expansion [35]. Ba–O bond is weaker than Ti–O and La–O bonds, which lead to larger TEC along *c*-axis. A high degree of anisotropy in thermal expansion could provide the capability of designing a coating with minimal residual stress by controlling the texture during manufacturing of the coating [30]. Furthermore, thermal expansion curves of BLT crystal show linear behavior with no sudden changes, implying that there is no first or second order phase transformation [36], which is in good agreement with the XRD results.

Fig. 10a shows specific heat curve of BLT by experimental measurement. When the temperature is below 700 °C, the specific heat changes gradually, but it begin to decline sharply when the temperature is above 700 °C. This conflicts with Debye equation, which suggests that the specific heat of ideal crystal increases with temperature and approaches constant at high temperature. Heat release of sample due to solid solution or crystallization during measurement, or the problem of equipment is possible cause. However, BLT exhibits good thermal stability according to XRD patterns recorded at

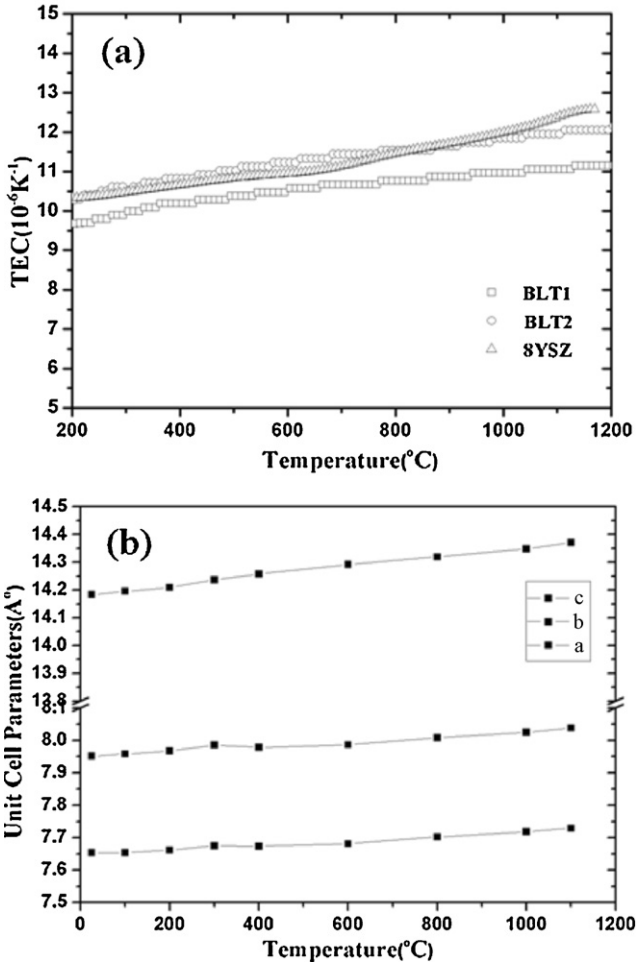

Fig. 9. Thermal expansion coefficients (a) and cell parameters (b) of BLT.

different temperatures. It can reasonably be inferred that abnormal variation in specific heat of BLT is caused by equipment problem. Therefore, the specific heats of BLT were calculated based on Neumann–Kopp law using Eq. (2), and the results are plotted in Fig. 10b. It can be seen that the specific heats of BLT increase with temperature.

Over a large extent temperature change, the density is not constant but is affected by temperature. The density at temperature T can be calculated using Eq. (3). The ρ_0 of BLT is 5.063 g/cm^3, α_a, α_b and α_c are given in Fig. 9b, and thus the densities of BLT at various temperatures are obtained, as shown in Fig. 11. It can be seen that the densities of BLT decrease linearly with temperature, and the values range from 4.85 to 5.06 g/cm^3 (25–1200 °C).

The thermal diffusivities of BLT3 and BLT4 are shown in Fig. 12a. It is found that the thermal diffusivities of BLT3 are lower than those of BLT4, the ratio of which is between 8:10 and 9:10, implying anisotropy in thermal diffusivity of BLT. The thermal diffusivities of BLT3 are in the range of 0.0050–0.0064 cm^2/s, while those of BLT4 are in the range of 0.0054–0.0074 cm^2/s (25–850 °C). The difference between thermal diffusivity of BLT3 and BLT4 is attributed to the insertion of Ba in BLT crystal. During the thermal diffusivity measurements of

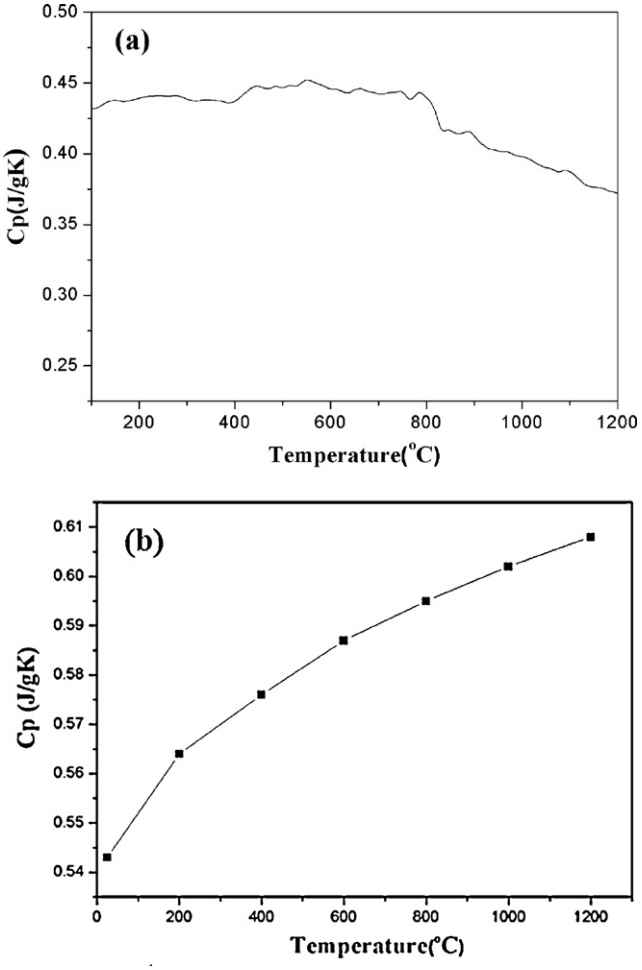

Fig. 10. Experimental measurement (a) and Neumann–Kopp (b) specific heat curve of BLT.

BLT3, the heat propagation direction is parallel to *c*-axis of BLT, thus the phonons are strongly scattered by Ba insertion layer, resulting in lower thermal diffusivity.

The thermal conductivity was calculated by Eq. (1), and the results are shown in Fig. 12b. It can be seen that the thermal conductivities of both BLT3 and BLT4 first decrease with the

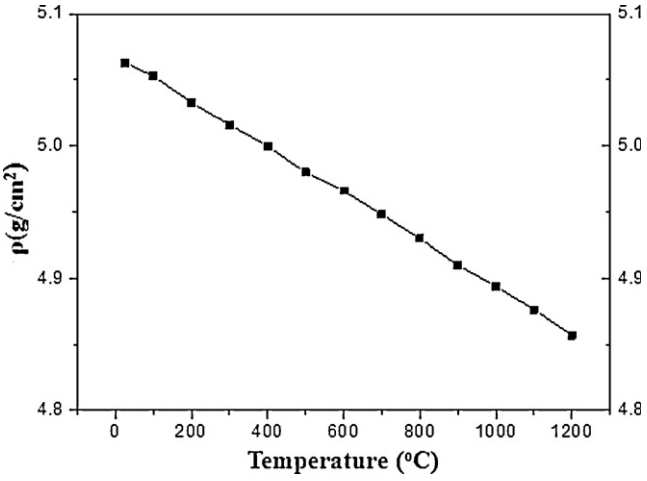

Fig. 11. The density curve of BLT.

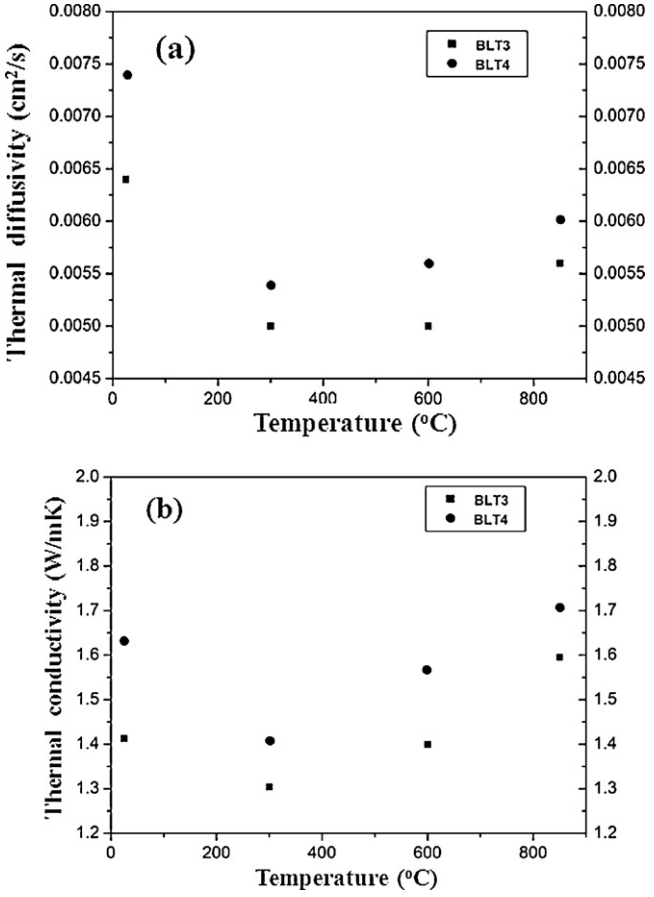

Fig. 12. Thermal diffusivities (a) and thermal conductivities (b) of BLT.

temperature below 300 °C, and then increase after 300 °C which is attributed to the radiative transport in the thermal flash test. The thermal conductivities of BLT3 are in the range of 1.31–1.60 W/mK, which are lower than those of BLT4 (1.41–1.71 W/mK). It is reported that the thermal conductivities of 8YSZ are in the range of 1.62–2.08 W/mK (25–850 °C) [37], which is higher than those of BLT. Especially, the thermal conductivity of BLT3 is lower than that of 8YSZ by nearly 20%. Therefore, BLT exhibits better thermal insulation performance than 8YSZ when used as thermal barrier coatings on hot section of advanced gas turbines.

The insertion of Ba leads to anisotropic crystal of BLT, and the crystalline anisotropy provide benefits for TBC applications in the form of better high temperature stability and improved thermo-physical properties when compared to 8YSZ. Detailed investigation on *c*-axis textured BLT has been carried out, indicating that BLT is a potential TBC material. Further work is directed to produce anisotropic BLT TBCs to exploit advantages of BLT material to the full.

4. Conclusions

$BaLa_2Ti_3O_{10}$ (BLT) powders and bulk material were produced by solid state reaction and hot pressing, respectively. After annealing at 1500 °C for 1 h, BLT bulk material exhibits *c*-axis textured structure, with *c*-axis parallel to the hot pressing direction. BLT shows excellent sintering resistance and exhibits

phase stability at 1500 °C for 110 h. BLT bulk material displays anisotropic performance. Thermal expansion coefficients of BLT in *a–b* plane are in the range from 9.5×10^{-6} to $11.3 \times 10^{-6}\,K^{-1}$, whereas those along *c*-axis are in the range of 10.4×10^{-6} to $12.1 \times 10^{-6}\,K^{-1}$, which are comparable to those of 8YSZ. Thermal conductivities of BLT along *c*-axis are in the range of 1.31–1.60 W/mK, which are nearly 20% lower than 8YSZ. These merits propose BLT as a potential TBC material, and our future work is directed to produce anisotropic BLT coatings aiming to exploit its comparative advantages in TBC applications.

Acknowledgments

This work was financially supported by the National Basic Research Program (973 Program) of China under grant No. 2010CB631200 and National Nature Science Foundations of China (NSFC, Nos. 50771009, 50731001 and 51071013).

References

[1] T.E. Strangman, Thermal barrier coatings for turbine airfoils, Thin Solid Films 127 (1985) 93–106.
[2] G.W. Goward, Progress in coatings for gas turbine airfoils, Surf. Coat. Technol. 108–109 (1998) 73–79.
[3] H.B. Guo, S.K. Gong, K.A. Khor, H.B. Xu, Effect of thermal exposure on the microstructure and properties of EB-PVD gradient thermal barrier coating, Surf. Coat. Technol. 168 (2003) 23–29.
[4] P.D. Harmsworth, R. Stevens, Phase composition and properties of plasma-sprayed zirconia thermal barrier coatings, J. Mater. Sci. 27 (1992) 611–615.
[5] G.D. Girolamo, C. Blasi, M. Schioppa, L. Tapfer, Structure and thermal properties of heat treated plasma sprayed ceria–yttria co-stabilized zirconia coatings, Ceram. Int. 36 (2010) 961–968.
[6] R. Vassen, X.Q. Cao, F. Tietz, D. Basu, D. Stöver, Zirconates as new materials for thermal barrier coatings, J. Am. Ceram. Soc. 83 (2000) 2023–2028.
[7] S. Guo, Y. Kagawa, Effect of thermal exposure on hardness and Young's modulus of EB-PVD yttria-partially-stabilized zirconia thermal barrier coatings, Ceram. Int. 32 (2006) 263–270.
[8] W. Ma, S.K. Gong, H.B. Xu, X.Q. Cao, The thermal cycling behavior of lanthanum–cerium oxide thermal barrier coating prepared by EB-PVD, Surf. Coat. Technol. 200 (2006) 5113–5118.
[9] W. Ma, S.K. Gong, H.B. Xu, X.Q. Cao, On improving the phase stability and thermal expansion coefficients of lanthanum cerium oxide solid solutions, Scripta Mater. 54 (2006) 1505–1508.
[10] W. Ma, S.K. Gong, H.F. Li, H.B. Xu, Novel thermal barrier coatings based on $La_2Ce_2O_7$/8YSZ double-ceramic-layer systems deposited by electron beam physical vapor deposition, Surf. Coat. Technol. 202 (2008) 2704–2708.
[11] Y. Wang, H.B. Guo, S.K. Gong, Thermal shock resistance and mechanical properities of $La_2Ce_2O_7$ thermal barrier coatings with segmented structure, Ceram. Int. 35 (2009) 2639–2644.
[12] D.R. Clarke, S.R. Phillpot, Thermal barrier coating materials, Mater. Today 8 (2005) 22–29.
[13] C. Cano, M.I. Osendi, M. Belmonte, P. Miranzo, Effect of the type of flame on the microstructure of $CaZrO_3$ combustion flame sprayed coatings, Surf. Coat. Technol. 201 (2006) 3307–3313.
[14] M. Pollet, S. Marinel, G. Desgardin, $CaZrO_3$, a Ni-co-sinterable dielectric material for base metal-multilayer ceramic capacitor applications, J. Eur. Ceram. Soc. 24 (2004) 119–127.
[15] S. Yamanaka, T. Maekawa, H. Muta, T. Matsuda, S. Kobayashi, K. Kurosaki, Thermophysical properties of $SrHfO_3$ and $SrRuO_3$, J. Solid State Chem. 177 (2004) 3484–3489.
[16] W. Ma, D.E. Mack, R. Vaßen, D. Stöver, Perovskite-type strontium zirconate as a new material for thermal barrier coatings, J. Am. Ceram. Soc. 91 (2008) 2630–2635.
[17] C.J. Howard, H.T. Stokes, Structures and phase transitions in perovskites – a group-theoretical approach, Acta Crystallogr. A61 (2005) 93–111.
[18] H. Lehmann, D. Pitzer, G. Pracht, R. Vassen, D. Stöver, Thermal Conductivity, Thermal expansion coefficients of the lanthanum rare-earth-element zirconate system, J. Am. Ceram. Soc. 86 (2003) 1338–1344.
[19] X.Y. Xie, H.B. Guo, S.K. Gong, H.B. Xu, Lanthanum–titanium–aluminum oxide: a novel thermal barrier coating material for applications at 1300 °C, J. Eur. Ceram. Soc. 31 (2011) 1677–1683.
[20] X.Y. Xie, H.B. Guo, S.K. Gong, H.B. Xu, Thermal cycling behavior and failure mechanism of $LaTi_2Al_9O_{19}$/YSZ thermal barrier coatings exposed to gas flame, Surf. Coat. Technol. 205 (2011) 4291–4298.
[21] Y.H. Wang, Z.G. Liu, J.H. Ouyang, H.Z. Liu, R.X. Zhu, Preparation and thermo-physical properties of $LaMgAl_{11}O_{19}$–$Yb_3Al_5O_{12}$ ceramic composites, Ceram. Int. 37 (2011) 2489–2493.
[22] R.M. Costescu, D.G. Cahill, F.H. Fabreguette, Z.A. Sechrist, S.M. George, Ultra-low thermal conductivity in W/Al_2O_3 Nanolaminates, Science 303 (2004) 989–990.
[23] C. Chiritescu, D.G. Cahill, N. Nguyen, D. Johnson, A. Bodapati, P. Keblinski, P. Zschack, Ultralow thermal conductivity in disordered, layered WSe_2 crystals, Science 315 (2007) 351–353.
[24] E.C. Subbarao, Crystal chemistry of mixed bismuth oxides with layer-type structure, J. Am. Ceram. Soc. 45 (1962) 166–169.
[25] Y. Shen, D.R. Clarke, P.A. Fuierer, Anisotropic thermal conductivity of the Aurivillus phase, bismuth titanate ($Bi_4Ti_3O_{12}$): a natural nanostructured superlattice, Appl. Phys. Lett. 93 (2008) 102907.
[26] S.N. Ruddlesden, P. Popper, On the crystal structure of the nitrides of silicon and germanium, Acta Crystallogr. 11 (1958) 465–468.
[27] F. Prado, L. Mogni, G.J. Cuello, A. Caneiro, Neutron powder diffraction study at high temperature of the Ruddlesden–Popper phase $Sr_3Fe_2O_{6+\delta}$, Solid State Ionics 178 (2007) 77–82.
[28] A. Olsen, R.S. Roth, Crystal structure determination of $BaNd_2Ti_3O_{10}$ using high-resolution electron microscopy, J.Solid State Chem. 60 (1985) 347–357.
[29] J.P. Guha, Synthesis, Characterization of barium lanthanum titanates, J. Am. Ceram. Soc. 74 (1991) 878–880.
[30] S. Sambasivan, K. Steiner, Patent no. US 6,680,126 B1, 2004.
[31] H.B. Guo, H.J. Zhang, G.H. Ma, S.K. Gong, Thermo-physical and thermal cycling properties of plasma-sprayed $BaLa_2Ti_3O_{10}$ coating as potential thermal barrier materials, Surf. Coat. Technol. 204 (2009) 691–696.
[32] B. Ihsan, P. Gregor, Thermochemical data of pure substances, VCH, Weinheim, Germany/New York, 1995.
[33] S.K. Chung, D.B. Thiessen, W.K. Rhim, A noncontact measurement technique for the density and thermal expansion coefficient of solid and liquid materials, Rev. Sci. Instrum. 67 (1996) 3175–3181.
[34] W.H. Rhodes, Agglomerate, Particle size effects on sintering yttria-stabilized zirconia, J. Am. Ceram. Soc. 64 (1981) 19–22.
[35] H.D. Megaw, Crystal structures and thermal expansion, Mater. Res. Bull. 6 (1971) 1007–1018.
[36] P. Arnold, L.G. Yaffe, The ε expansion and the electroweak phase transition, Phys. Rev. D 49 (1994) 3003–3032.
[37] Y.L. Zhang, L., Guo, H.B., Guo, S.K. Gong, Chin. J. Aeronautics (in press).